

Article

Rapid Impedance Measurement of Lithium-Ion Batteries Under Pulse Ex-Citation and Analysis of Impedance Characteristics of the Regularization Distributed Relaxation Time

Haisen Chen ¹, Jinghan Bai ¹, Zhengpu Wu ¹, Ziang Song ¹, Bin Zuo ¹, Chunxia Fu ², Yunbin Zhang ³ and Lujun Wang ^{2,*}

¹ Hubei Key Laboratory for High-Efficiency Utilization of Solar Energy and Operation Control of Energy Storage System, Hubei University of Technology, Wuhan 430068, China; c2028987060@163.com (H.C.); baijinghan@hbust.edu.cn (J.B.); w13298128043@163.com (Z.W.); songziang1999@163.com (Z.S.); zuobin1777@163.com (B.Z.)

² Powerchina Equipment Research Institute Co., Ltd., Wuhan 430068, China; fuchunxia7192@163.com

³ Hubei New Energy Co., Ltd., Wuhan 430068, China; zhangyunbin123456@163.com

* Correspondence: wanglujun@zju.edu.cn; Tel.: +86-1532-731-2005

Abstract: To address the limitations of conventional electrochemical impedance spectroscopy (EIS) testing, we propose an efficient rapid EIS testing system. This system utilizes an AC pulse excitation signal combined with an “intelligent fast fourier transform (IFFT) optimization algorithm” to achieve rapid “one-to-many” impedance data measurements. This significantly enhances the speed, flexibility, and practicality of EIS testing. Furthermore, the conventional model-fitting approach for EIS data often struggles to resolve the issue of overlapping impedance arcs within a limited frequency range. To address this, the present study employs the Regularization Distributed Relaxation Time (RDRT) method to process EIS data obtained under AC pulse conditions. This approach avoids the workload and analytical uncertainties associated with assuming equivalent circuit models. Finally, the practical utility of the proposed testing system and the RDRT impedance analysis method is demonstrated through the estimation of battery state of health (SOH). In summary, the method proposed in this study not only addresses the issues associated with conventional EIS data acquisition and analysis but also broadens the methodologies and application scope of EIS impedance testing. This opens up new possibilities for its application in fields such as lithium-ion batteries (LIBs) energy storage.

Keywords: electrochemical impedance spectroscopy; regularization distributed relaxation time; intelligent fast fourier transform; AC pulse excitation; lithium-ion batteries; state of health



Academic Editor: Sylvain Franger

Received: 13 December 2024

Revised: 22 February 2025

Accepted: 25 February 2025

Published: 27 February 2025

Citation: Chen, H.; Bai, J.; Wu, Z.; Song, Z.; Zuo, B.; Fu, C.; Zhang, Y.; Wang, L. Rapid Impedance

Measurement of Lithium-Ion Batteries Under Pulse Ex-Citation and Analysis of Impedance Characteristics of the Regularization Distributed Relaxation Time. *Batteries* **2025**, *11*, 91. <https://doi.org/10.3390/batteries11030091>

Copyright: © 2025 by the authors. Licensee MDPI, Basel, Switzerland. This article is an open access article distributed under the terms and conditions of the Creative Commons Attribution (CC BY) license (<https://creativecommons.org/licenses/by/4.0/>).

1. Introduction

In the realm of new energy generation, the intermittency, volatility, and randomness inherent in the process necessitate the integration of energy storage for stable operation. Electrochemical energy storage, acknowledged for its economic benefits, stands as a widely employed form of energy storage. However, it is accompanied by safety risks and degradation issues. LIBs commonly used for energy storage are essentially electrochemical systems, and their impedance characteristics are closely linked to the operational state of the batteries [1,2]. Consequently, EIS provides an effective means for in-depth exploration of internal impedance characteristics and operational states within batteries [3,4].

The measurement of EIS can be categorized into two methods: frequency-domain and time-domain [5,6]. The former is often conducted in electrochemical workstations through frequency sweeping, and it is time-consuming and relatively costly, making it impractical for real-world application scenarios [7–9]. Angst et al. employed a dual-oscilloscope-based Lissajous analysis method for impedance acquisition. The advantage of this method lies in its ability to perform accurate measurements across both high- and low-frequency ranges, while effectively suppressing electrical noise in the system. The drawback of this approach is its susceptibility to noise interference at high frequencies and relatively poor accuracy at low frequencies [10]. The time-domain measurement method involves converting time-domain signals into frequency-domain data using algorithms, coupled with mathematical computations to obtain impedance information. In order to enhance the efficiency of impedance measurements within the time-domain measurement method, optimization of excitation signals and algorithms is often employed. For instance, Hoshi et al. successfully reduced the duration of the excitation signal by utilizing the WT in conjunction with a step signal [11]. Similarly, Arora et al. applied a step signal to the equivalent circuit model and transformed the response into *s*-domain through Laplace transform to obtain the model impedance [12]. However, the signal extraction accuracy across different frequency ranges may be affected by the choice of wavelet, while the charging and discharging processes of step signals could lead to a shift in the battery's static operating point, thereby impacting the test results. Peter et al. proposed a time-domain analysis method for electrochemical impedance spectroscopy (EIS) based on ordinary least squares (OLS), demonstrating the high accuracy and consistency of the method over a wide frequency range [13]. However, the accuracy of time-domain measurements is influenced by experimental parameters such as excitation direction and charge amount, and the method's applicability may be limited in extreme frequency ranges or nonlinear systems. To avoid the above-mentioned drawbacks, Kallel et al. proposed an optimized multi-sine excitation signal for battery impedance measurement, which significantly improved the measurement stability and accuracy in the low-frequency range while reducing the measurement time [14]. This method can reduce measurement time and maintain high accuracy, but it requires higher demands on the reference signal and hardware. Moreover, the additional signal generation device, along with the complex system implementation and signal synchronization, increases its practical complexity. Bullecks et al. proposed a rapid impedance measurement method based on chirp signals, using instantaneous frequency definition and chirp input signals to achieve impedance measurement over a wide frequency range, significantly improving measurement speed and noise immunity. However, the method relies on the assumption of a linear system, and experimental validation has not yet fully covered real electrochemical systems [15]. At the same time, Du et al. proposed an enhanced excitation signal based on a double pseudo-random sequence (DPRS) and combined it with a weighted bilateral filter (WBIF) method for impedance measurement, significantly improving the measurement accuracy and robustness [16]. However, the signal generation and processing are relatively complex. Additionally, this method relies on specific hardware configurations, such as data acquisition devices and signal injection systems, which may limit its effectiveness if the hardware conditions are insufficient. Therefore, we can conclude that the frequency-domain measurement method is challenging to apply outside the laboratory setting. On the other hand, the time-domain measurement method requires specific signal generation and algorithm processing, making the selection of appropriate excitation signals and processing algorithms crucial for its practical implementation. To address the issues with the excitation signal mentioned above, this paper considers various signal types and the practical usage scenarios of batteries and selects alternating current (AC) pulse signals as the excitation. The selection of AC pulse signals serves a dual purpose: Firstly, it

ensures that the battery's static operating point remains undisturbed during the testing process, thereby guaranteeing data accuracy. Secondly, this signal, when transformed from the time-domain to the frequency-domain, can contain a greater amount of impedance information, thereby enhancing measurement speed. Additionally, the choice of pulse signals enables the integration of the testing system into power and switching circuits, further improving practicality.

The impedance data of the battery obtained through EIS measurement can provide important information for SOH estimation. However, the time constants of the internal chemical and physical reaction processes of the battery are similar, leading to significant overlap in the semicircular portion of the EIS plot [17]. This complicates data fitting and feature extraction, thereby influencing the estimation of SOH [18]. Chang et al. compared EIS fitting data from various equivalent models and then selected the data from the more precise fitting models for SOH estimation [19]. On the other hand, Huang et al. introduced a state-space moving impedance model, encompassing three scales of lithium-ion impedance models: single particle, bulk, and porous electrode scales [20]. This model offers high precision but demands advanced parameter identification and data computation. It also requires a priori assumptions about the electrode system.

In summary, due to the overlap of the impedance arc portion in the EIS data and the difficulty in determining the relative merits of fitting models, it is often challenging to obtain ideal fitting results, which in turn affects the estimation of battery SOH. To address this issue, we adopted the RDRT method to process the EIS impedance data. This method can directly distinguish the time constants corresponding to different electrochemical reaction processes and their approximate frequency ranges. Unlike traditional EIS fitting methods, the RDRT method does not require consideration of the relative merits of different fitting models, significantly reducing the workload and uncertainty in analysis. Moreover, it does not rely on prior knowledge of the research subject, providing a more efficient and reliable EIS analysis technique.

To address the challenges in EIS excitation signals, data analysis, and practical applications, this paper proposes an EIS testing system based on pulse excitation signals, combined with the RDRT analysis method, aimed at quickly and accurately measuring battery impedance characteristics to provide reliable data support for SOH estimation. Through theoretical derivation, the feasibility and advantages of the pulse excitation signal are detailed, and the principles of the RDRT method in EIS are analyzed, demonstrating its ability to effectively resolve the overlap issue inherent in traditional methods, thereby reducing reliance on complex fitting models. This paper designs a rapid EIS testing system based on a variable excitation balancing board, introducing the hardware and software implementation, and experimentally validating the feasibility of the system. Health state estimation experiments further confirm the effectiveness of the testing system and the RDRT analysis method. Overall, this work not only provides a new approach for rapid acquisition of lithium-ion battery impedance, but also addresses the limitations of traditional EIS analysis methods, broadening its applications in fields such as energy storage stations and new energy vehicles, and advancing the precise monitoring and health state assessment of battery management systems.

2. Measurement of EIS Data and Analysis of the DRT Principle

2.1. Principles of Conventional EIS Data Testing

Conventional EIS testing employs sinusoidal excitation signals within a frequency range of 0.1 to 1 kHz [21,22], which widely covers impedance information associated with various polarization processes [23,24]. Low-frequency measurements typically require a longer time. Traditional methods can measure down to 0.1 Hz without such extended

duration, and existing instruments offer various methods to respond to signals below 0.1 Hz [25]. In conventional time-domain EIS testing, multiple cycles of a single-frequency sinusoidal signal scan are conducted to ensure accuracy, coupled with the use of Discrete Fourier Transform (DFT) for data processing. The schematic diagram of conventional EIS testing is illustrated in Figure 1A.

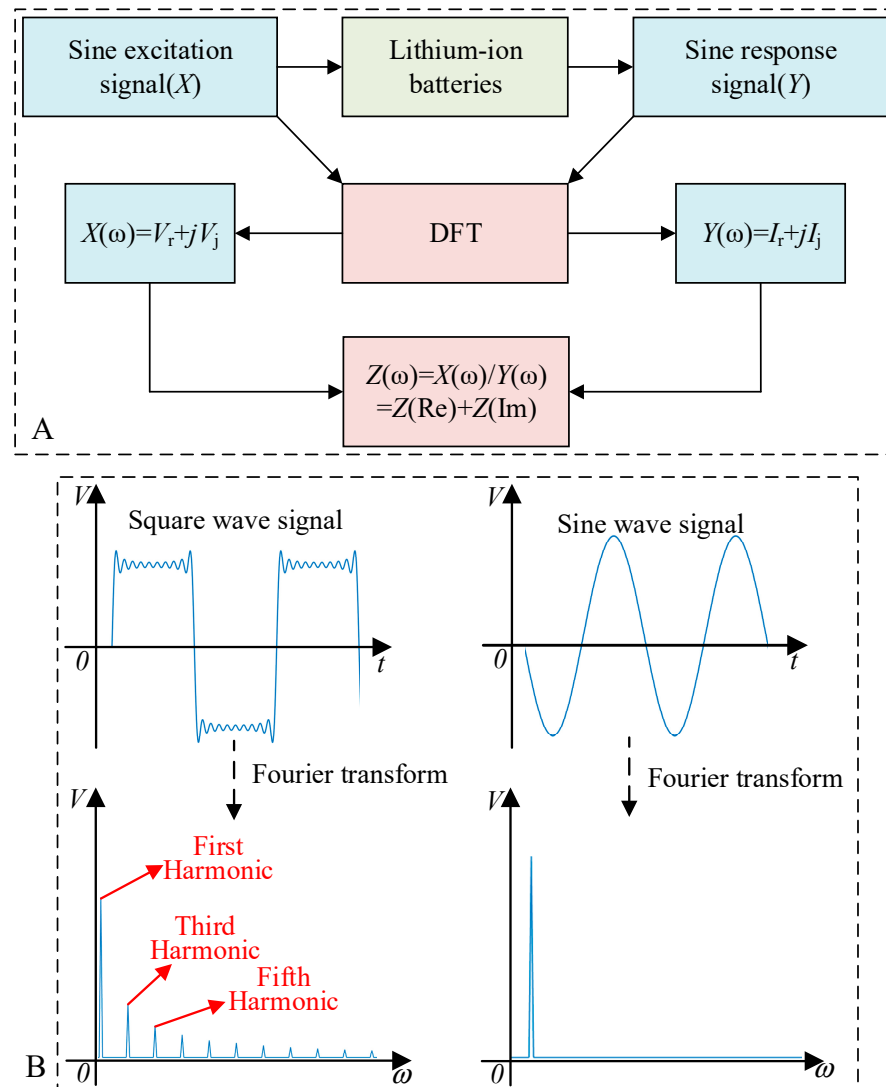


Figure 1. EIS data principle test graph. (A) Schematic diagram of conventional EIS testing; (B) Comparative analysis of pulse signal and sine wave signals through fourier decomposition.

2.2. Investigation of EIS Testing Under Pulse Signal

Given the practical significance of time-domain measurement methods and the frequent integration of batteries with power electronic circuits, this paper proposes the use of pulse excitation signals to replace traditional sinusoidal signals. When pulse excitation signals are used for impedance testing, they are periodic signals, which, according to the definition of fourier series, can be expanded into a sum of trigonometric functions. Additionally, a single-frequency pulse signal can be decomposed through fourier series into a sum of odd harmonic components of sine waves [26]. Furthermore, the selection of pulse excitation signals better aligns with the operating conditions of power switching circuits, thereby significantly enhancing their practicality and integrability.

As shown in Figure 1B, the information content in the frequency domain obtained from the pulse signal after fourier transform is significantly greater than that from the

sine wave signal. This indicates that using pulse excitation signals for impedance testing can yield more response information at a single frequency point, thereby achieving rapid “one-to-many” impedance measurement. In subsequent impedance measurements, AC pulse signals will be chosen, which can effectively address the issue of data accuracy caused by battery potential shifts. For details, see Section 4.2.

2.3. EIS Analysis Based on the DRT Method

The DRT can be understood as the time required for a transient variable within an electrode system to tend toward a steady state. It is commonly represented by characteristic time constants, τ . Smaller τ values correspond to shorter transition times from transient to steady state, and conversely, larger τ values indicate longer transition times. Since different electrochemical processes correspond to different relaxation times, DRT can be employed to discern different electrochemical processes. Its advantage lies in the fact that it does not require prior knowledge or assumptions about the presence of multiple characteristic time constants within the testing system [27,28]. As shown in Figure 2, it illustrates the electrochemical model of LIBs and the DRT equivalent circuit model.

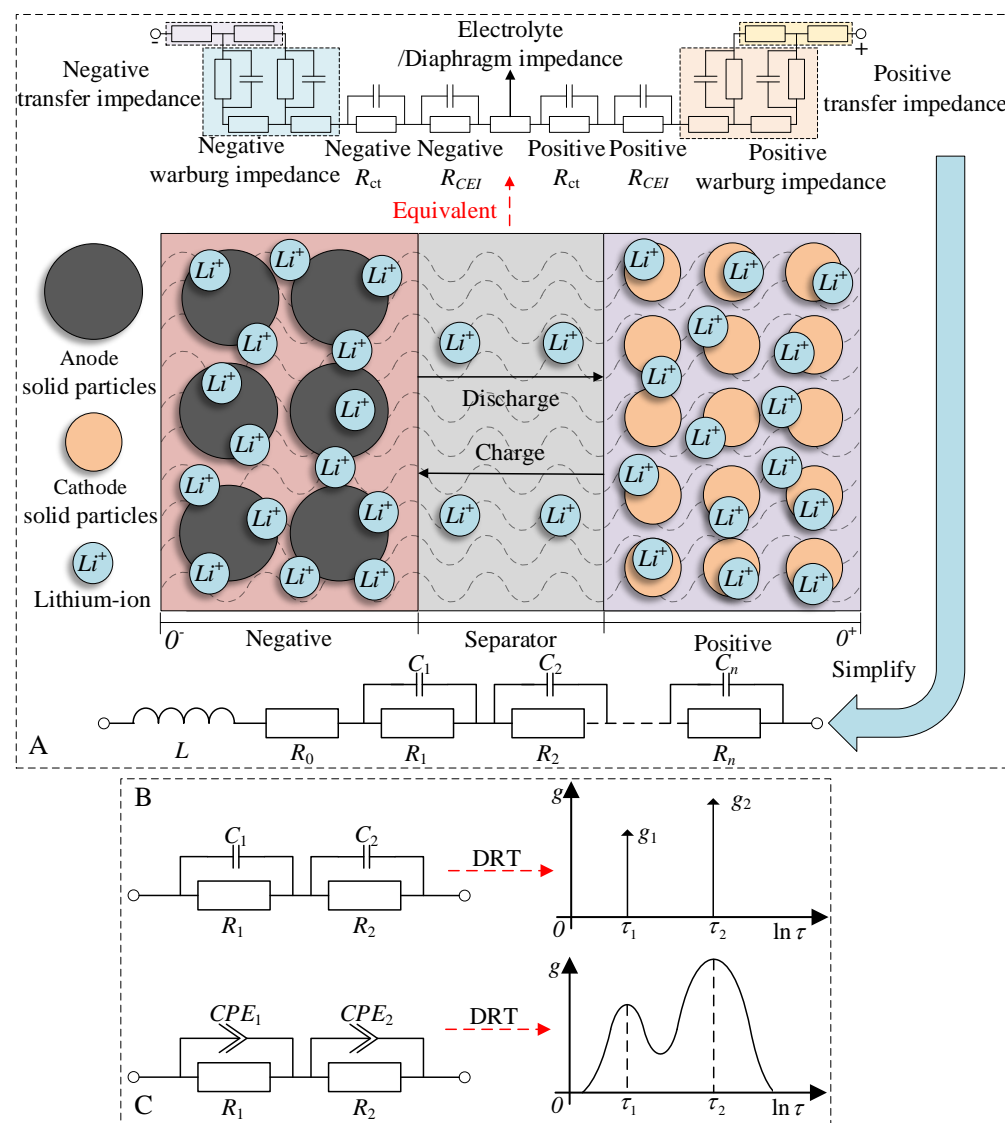


Figure 2. EIS data DRT method analysis graph. (A) Electrochemical model of LIBs and DRT equivalent circuit model; (B,C) Comparative analysis of ideal elements and CEP after DRT processing.

From Figure 2A, it is evident that LIBs constitute a relatively intricate capacitive electrochemical system. Its electrode reaction process is a composite procedure encompassing a series of steps, including material transport and charge transfer [29]. This can be equivalently represented through electronic devices, with the primary and most significant components being the series and parallel combination of resistance and capacitance. For the DRT method, the electrochemical system is regarded as an ohmic resistor R_0 (where inductors can be added) connected in series with multiple polarization processes. This method can achieve coverage of any electrochemical system impedance model [30], and a single polarization process can be represented by the parallel connection of capacitors and resistors. To more intuitively reflect the different electrochemical reactions of LIBs, a simplified model shown in Figure 2A can be used to represent it.

The ideal polarization process of a single component can be described by a parallel $R//C$ combination, as represented by the Dirac delta function in Figure 2B. However, the electrode system undergoes a non-ideal polarization process. To better reflect the polarization process of lithium-ion batteries, the Constant Phase Element (CPE) is commonly used to replace the capacitive component, forming the $R//CPE$ model, which is represented by a relaxation time distribution function centered around the characteristic time constant, as shown in Figure 2C. Figure 2B,C illustrates the comparison between the ideal components and the CPE after DRT processing. For the subsequent DRT processing of EIS data and the extraction of characteristic data for SOH estimation, the equivalent polarization process under the $R//CPE$ model is employed.

2.4. Regularization-Based DRT Analysis

The core of data analysis using the DRT method is based on the existing EIS impedance testing data. Through the algorithm, the distribution function of the characteristic time constants, $g(\tau)$, is obtained, thereby revealing the polarization processes or kinetic information of the electrochemical system [31,32]. After processing with the DRT method, the EIS frequency range is commonly divided logarithmically. Its impedance expression can be represented as follows:

$$\begin{cases} \tau = f(\ln \tau) e^{\ln \tau}, G(\tau) = \tau \cdot g(\tau) \\ Z(f) = Z_L + R_0 + R_{pol} \int_0^\infty \frac{G(\tau)}{1 + j2\pi f \tau} d \ln \tau \end{cases} \quad (1)$$

From the above equation, it is evident that the distribution function $g(\tau)$ is an inverse problem, and $g(\tau)$ can be sensitive and unstable in experimental testing. To address this challenge, several methods have been developed, including regularization techniques and Fourier transform methods [33,34]. Among these, regularization methods are favored for their simplicity, noise robustness, and adjustability. The following section will provide a detailed introduction to it.

Regularization is a general technique used to solve ill-posed problems or overfitting issues by incorporating additional information into the target problem for adjustment. The regularization equation can be expressed in the following form:

$$\sum_{n=1}^N [y_n - g(x_1, x_2, \dots, x_M, f_n)]^2 + \lambda h(x_1, x_2, \dots, x_M) \quad (2)$$

In the above equation, f_n represents the frequencies corresponding to the sampled points, N is the number of sampled points, y_n denotes the experimental test data at a specific frequency, $g(x_1, x_2, \dots, x_M, f_n)$ is the fitting function, λ is the regularization parameter, and $\lambda \geq 0$, $h(x_1, x_2, \dots, x_M)$ is the penalty function, where x_M represents the weights of the terms in the fitting function. Equation (2) reveals that the quality of the regularization

fit depends on N and λ . If λ is too small, it increases the complexity of the model and may lead to function oscillations, while if it is too large, it can result in underfitting due to information loss. The derivation process of applying RDRT to process EIS data is as follows: First, discretize $G(\tau)$:

$$G(\tau) = \sum_{n=1}^N x_n \phi_n(\ln \tau) \quad (3)$$

Subsequently, the weight parameters x_n are determined, and they are linearly combined with the discrete basis functions $\phi(\ln \tau)$ to obtain the reconstruction parameters of DRT [30,31]. Simultaneously, by combining Equation (3), a discretized fitting model can be obtained:

$$Z(X, f) = Z_L + R_0 + \sum_{n=1}^N \left[x_n \left(R_{pol} \int_0^\infty \frac{1}{1 + j2\pi f \tau} \phi(\ln \tau) d \ln \tau \right) \right] + e_z(f) \quad (4)$$

In the equation, $e_z(f)$ represents discretization error, and the variables x_n can be estimated by minimizing the objective function $h(X)$:

$$h(X) = \sum_{m=1}^M [Z_{exp}(f_m) - Z(X, f)]^2 \quad (5)$$

where $Z_{exp}(f_m)$ is the measured data of EIS, $Z(X, f)$ is the simulated impedance spectrum, and $X = (x_1, x_2, \dots, x_n)$. $h(X)$ is also sensitive to measurement errors and can be redefined with the introduction of regularization as follows:

$$h(X) = \sum_{m=1}^M [Z_{exp}(f_m) - Z(X, f)]^2 + \lambda P(X) \quad (6)$$

Through the derivation process outlined above, we can observe that the penalty function $P(X)$ serves as the constraints on the initial objective function. The optimal X can be determined when the contours of the objective function first intersect with $P(X)$ in the graphical representation. Additionally, different forms of $P(X)$ correspond to different regularization methods, such as Lasso [31], and Ridge [32,35], among others.

In summary, the regularization method employed in DRT utilizes penalty terms to control model complexity, thereby optimizing the fitting quality. When addressing practical issues, it is necessary to adjust the number of sample points and the regularization parameter based on the data characteristics to achieve the best fitting results. In the subsequent sections of this paper, a continuous-discrete Gaussian RDRT approach will be used for data fitting. The EIS data processed using the RDRT method further improved the accuracy of SOH estimation, providing a more reliable tool for battery state monitoring in practical applications.

3. EIS Testing System Design

3.1. Overall Structure of the Testing System

The existing EIS testing techniques primarily rely on electrochemical workstations, which suffer from drawbacks such as slow impedance testing speed, limited flexibility, a singular operational mode, and challenges in practical applications. In response to these issues, this paper proposes an EIS rapid testing system based on a variable excitation balance board. This system provides a research framework for the practical application of fast EIS acquisition in lithium-ion batteries, overcoming current technological limitations

in terms of practicality. It exhibits higher testing efficiency and flexibility for real-world applications. The system structure is illustrated in Figure 3A.

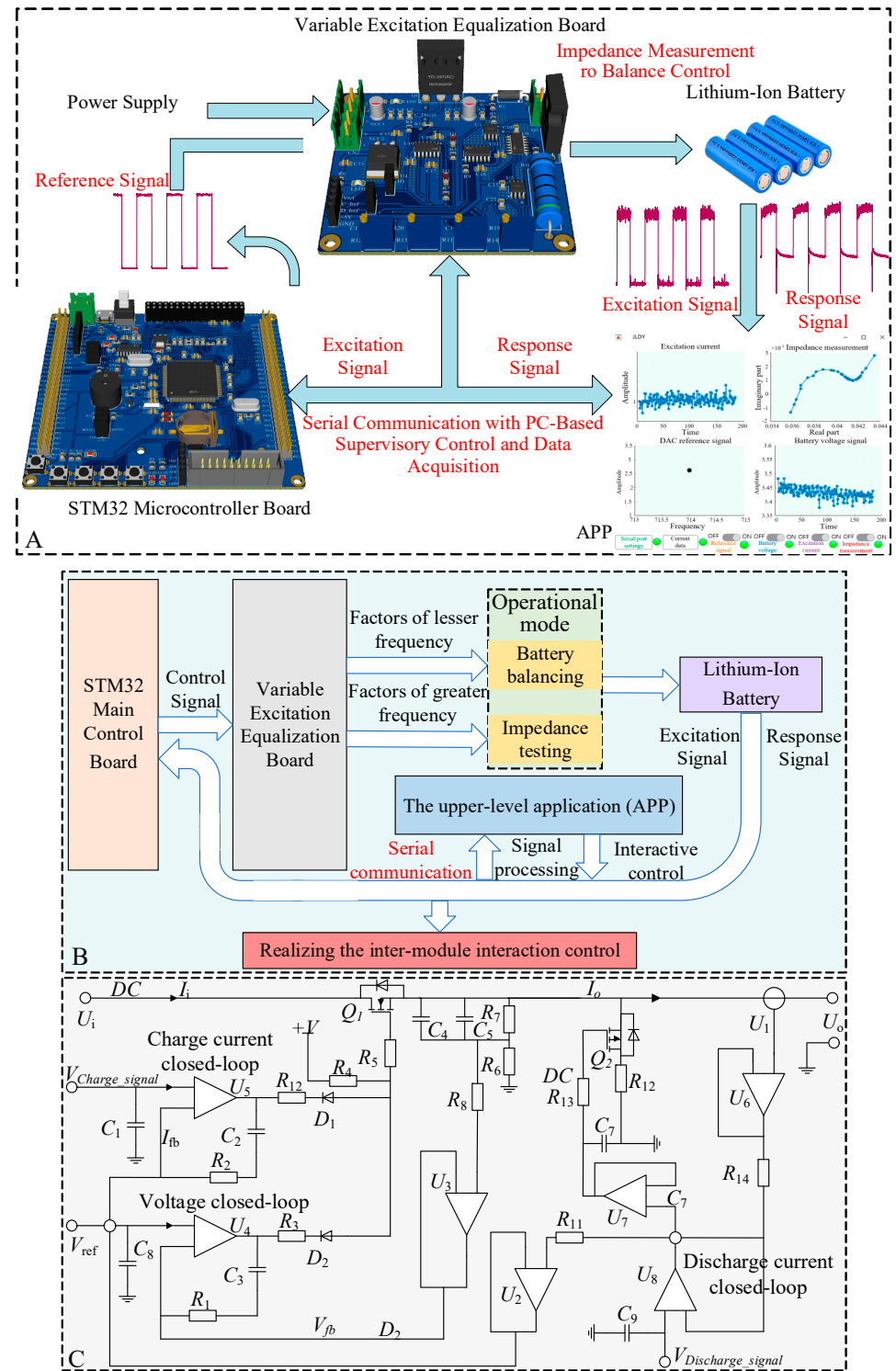


Figure 3. Hardware architecture diagram of the EIS rapid testing system. (A) Overall architecture diagram of the EIS rapid testing system; (B) Hardware operational structure diagram of the impedance testing system; (C) Topology diagram of the variable excitation equalization board.

The structure of this testing system comprises four main components: LIBs, the variable excitation balancing board, the STM32 main control board, and the upper-level PC application (APP). The operational process is as follows: First, the STM32 main control

board sends instructions to the variable excitation balancing board via control signals, specifying parameters such as the type, amplitude, and frequency of the excitation signal. Simultaneously, the variable excitation balancing board sets the voltage limit based on the type of object being tested (typically around 4.5 V for LIBs). Furthermore, the STM32 main control board uploads data to the upper-level PC application through a serial connection, where data processing and real-time monitoring and display of the testing system occur. In the following sections, we will provide a detailed overview of the system's various modules and impedance testing experiments.

3.2. Hardware Introduction of the Testing System

The system hardware comprises two main components: the STM32 main control board and the variable excitation balance board, as depicted in Figure 3B. The STM32 main control board employs a STM32F407 as its core, with peripheral circuits and board shape redesigned according to the testing system requirements. It features buttons, an LCD screen, serial communication (baud rate set at 256,000), high-precision AD acquisition (maximum error $\pm 0.1\%$, maximum sampling frequency 2.4 M), and DA output capabilities. The buttons are used to adjust the amplitude and frequency of the output control signal. The LCD is utilized to display excitation signals, battery voltage, current, and other information. Serial communication is employed to upload reference signals, excitation signals, and response signals to the upper-level computer application for data processing and real-time display. Figure 3B provides an overview of the overall structure of the hardware modules.

Figure 3C depicts the fundamental topology circuit of the variable excitation balance board, which serves as the core for generating excitation signals in this testing system. The basic control elements include: MOSFET Q_1 , responsible for controlling the charging of LIBs; MOSFET Q_2 , in charge of discharging; current reference source provided by U_1 ; and voltage reference source provided by resistors R_6 and R_7 . The primary charging and discharging control logic is as follows: when the control signal V_{Charge_singal} exceeds the reference signal, MOSFET Q_1 opens to apply the charging control signal to LIBs. Conversely, MOSFET Q_2 opens, working in conjunction with R_{12} , to discharge the battery. Furthermore, the signal types, amplitudes, and frequency levels for LIBs charging, discharging, and impedance testing are determined by V_{Charge_singal} and $V_{Discharge_singal}$. In addition, the topology structure incorporates overvoltage protection. By using the voltage divider structure of R_7 and R_6 , V_{fb} is obtained. The combination of resistor R_4 with the secondary diodes D_1 and D_2 implements an “OR” control logic. By adjusting the size of V_{ref} , output voltage U_o can be constrained, thereby achieving the desired output protection.

The variable excitation balance board falls into the category of linear control rather than switch control. The advantages of linear control can be elucidated from two aspects: Firstly, in terms of response time, it can achieve responses in the order of microseconds. Secondly, it offers a high degree of variability in control. On one hand, it allows for the free adjustment of the amplitude, frequency, and the type of excitation signal. On the other hand, it provides the capability for mode selection through programmable control, in conjunction with the functions of both the charge–discharge unit and the electrochemical workstation. This setup can even serve as an option for battery balancing groups. In summary, the variable excitation balance board employs a dual closed-loop structure for both voltage and current, successfully achieving a “current control, voltage limiting” output mode. Additionally, it allows for the flexible alteration of the type, frequency, and amplitude of the output signal. This hardware design significantly broadens the applicability and practicality of EIS testing. This enables the rapid and accurate collection of EIS data, providing the necessary foundation for SOH estimation. Subsequently, we will proceed with an introduction to the software component, building upon the foundation of the hardware system.

3.3. Software Introduction of the Testing System

The system software is divided into two parts: the lower-level control implemented on the STM32 microcontroller and the upper-level computer application (APP), as illustrated in Figure 4. Figure 4A depicts the structural diagram of the software components within the testing system. Initially, the STM32 microcontroller controls the excitation power supply's operating mode, output signal type, amplitude, and frequency. Simultaneously, it collects the excitation current from the battery and the corresponding response voltage, transmitting these signals via a serial interface to the upper-level computer for real-time status display and data processing. Figure 4B represents the structural principles of impedance data processing within the upper-level computer application. Initially, it receives data transmitted through the serial interface and subsequently employs the IFFT to convert the originally time-domain signals into frequency-domain signals. Finally, through mathematical formulas and data point optimization, the ultimate EIS plot is obtained.

It is important to note that during data processing, the signal frequency varies. According to the Nyquist sampling theorem, the sampling frequency (F_s) must be at least twice the maximum frequency (f_{max}), i.e., $F_s \geq 2 f_{max}$, to ensure that the frequency data of the sampling points do not overlap during data processing [36]. Additionally, in the original FFT algorithm, data acquisition depth and data length change due to different data frequencies, resulting in a mismatch between the original time-domain data and the frequency-domain data after FFT processing. This mismatch hinders subsequent quantitative analysis of data and impedance data calculation. To address this issue, we have improved the original FFT algorithm and proposed the “intelligent FFT optimization algorithm”. This algorithm optimization involves the use of a small-range mean and data acquisition depth optimization. Its formula is as follows:

$$\left\{ \begin{array}{l} F_s = \frac{1}{T_{f_{i+1}} - T_{f_i}}, \quad T_{f_i} = \frac{\sum\limits_m^{N/n} t_i}{N/n} \\ N'_i = \frac{\sum\limits_m^{N/n} N_m}{N/n}, \quad m = 1 + (N/m) \cdot (i - 1) \end{array} \right. \quad (7)$$

where t_i represents a data point in the time domain during data collection, T_{f_i} represents a recalculated data point after data collection, F_s is the sampling frequency, N is the data length within the time domain during data collection, $i = 0, 1, 2, 3 \dots$ denotes natural numbers, n represents the predetermined data length that needs to be processed, N/n is the data length of each portion after partitioning, N_m is the initial data point collected, and N'_i is the new data point after processing. The approach employed by the aforementioned algorithm is as follows: Given the current data length and data acquisition depth obtained from the raw data, they are subdivided into small ranges, and these subdivided data are then combined to yield new data. This ensures the effective resolution of issues related to inconsistent data acquisition depth and inaccurate correspondence between time-domain and frequency-domain data points, thereby providing essential prerequisites for subsequent impedance calculations.

Following the processing with the IFFT, the frequency-domain data points of the excitation signal and response signal are more numerous and exhibit a gradually decreasing trend. Ideally, in the frequency domain, the data should only peak at odd harmonics. However, due to the presence of interference and other factors, even-frequency points may also appear. To ensure the accuracy of impedance data, we only select the first few odd harmonics as data points for impedance calculation. Additionally, according to the Kramers–Kronig theorem, impedance measurements between individual frequency

points are unaffected and can be removed [37,38]. Alternatively, appropriate smoothing algorithms can be incorporated into the data processing to obtain the final impedance data.

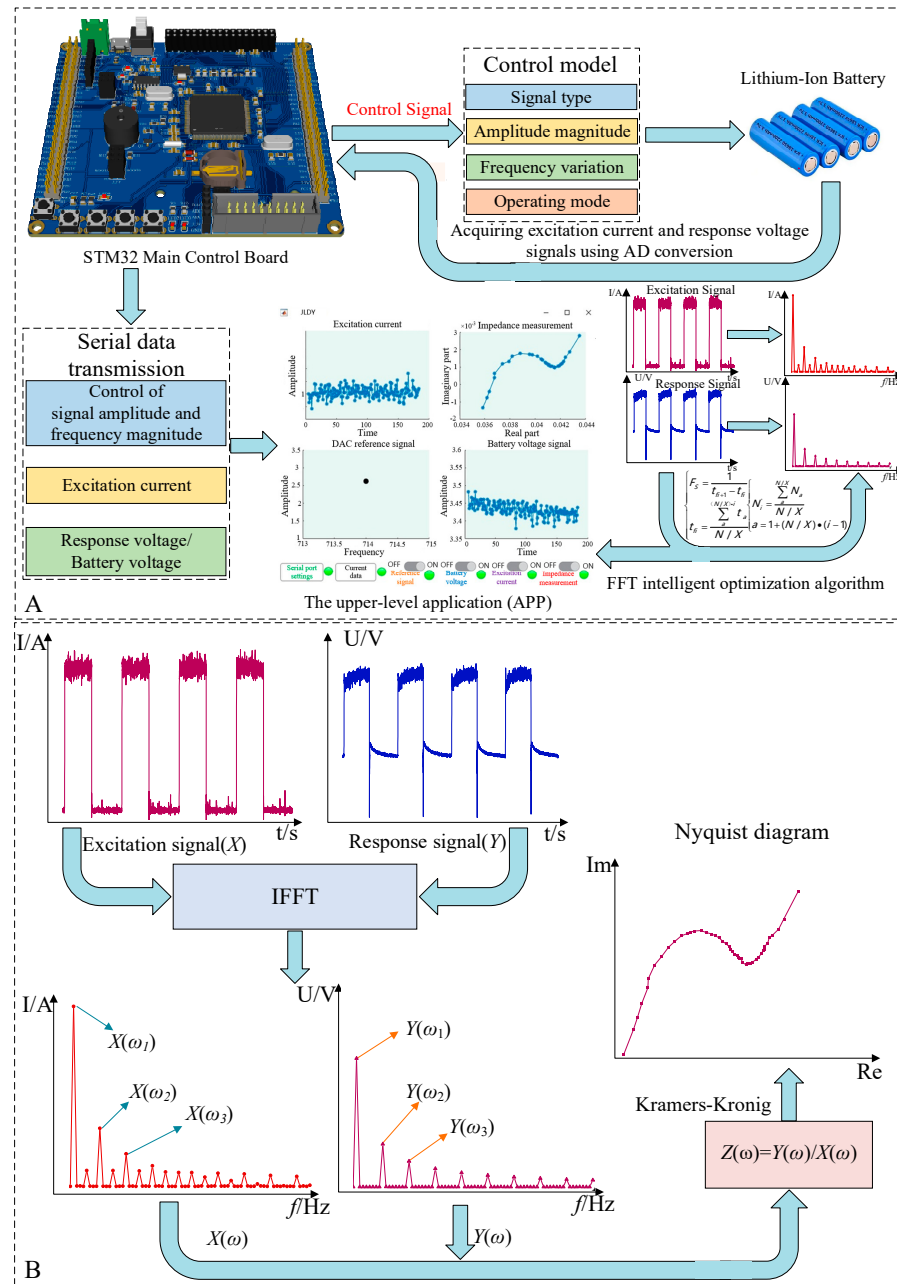


Figure 4. Software architecture diagram of the EIS rapid testing system. (A) Schematic diagram of the software architecture of the system; (B) Structural diagram of the data processing module in the upper-level application.

4. EIS Test Experiment

4.1. Experimental Subjects and Preprocessing

The experimental subject is a lithium-ion battery of the 18650 model, specifically the INR18650-26E variant, with the following specifications: a rated capacity of 2.55 Ah, a rated voltage of 3.65 V, a charging cut-off voltage of 4.25 V, a discharge cut-off voltage of 2.7 V, and an initial internal resistance of approximately 40 mΩ. The battery uses nickel–cobalt–manganese (NCM) as the cathode material and graphite as the anode material. The electrolyte is a liquid organic electrolyte, typically composed of lithium salts (such as LiPF₆) and organic solvents (such as dimethyl carbonate and ethylene carbon-

ate). These materials ensure the battery's high energy density and stable charge–discharge performance. In this experiment, an aging test will be conducted on the battery, with impedance measurements taken at various stages of the aging process. Additionally, in accordance with the national standard GB/T18287-2000 [39], the requirement for cycle life testing involves charging and discharging the battery at 1C rate in an ambient temperature of $(20 \pm 5)^\circ\text{C}$ until two consecutive discharge durations fall below 36 min, which is considered the end of life. The cycle life of the battery should be no less than 300 cycles. Therefore, in this experiment, the aging cycle count for the lithium-ion battery has been set at 350 cycles. The aging experiment of the lithium-ion battery is depicted in Figure 5A–C.

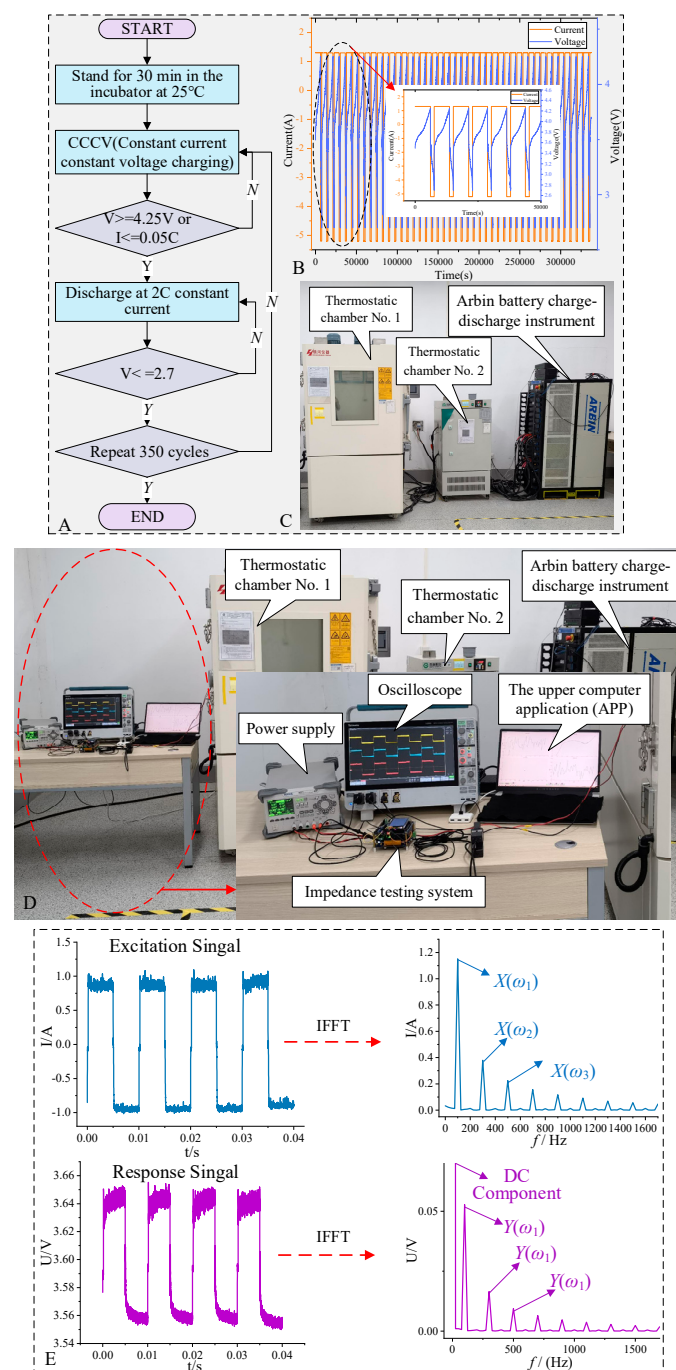


Figure 5. Lithium-ion battery aging and impedance testing experimental graph. (A) Flowchart of the LIBs aging experiment; (B) Voltage and current variation chart of the aged LIBs during the aging test; (C) Experimental graph of actual aging test for LIBs; (D) Experimental graph of actual testing on LIBs; (E) Experimental signal graph of EIS testing at 100 Hz.

Figure 5A presents the flowchart of the aging cycles for LIBs. Each group of tests consists of 50 cycles, and impedance tests are conducted after every 50 aging cycles. Figure 5B illustrates the voltage and current variations in LIBs during the aging test. Figure 5C provides an actual representation of the aging experiment with the battery placed inside temperature chamber number 1.

4.2. Experimental EIS Testing Under AC Pulse Signal

To ensure the controllability of impedance testing experiments, the lithium-ion battery was still placed in a constant temperature chamber at 25 °C. The actual EIS testing of LIBs under AC pulse signals is depicted in Figure 5D,E. Figure 5D shows the actual EIS testing of LIBs under AC pulse signals, while Figure 5E provides a comparison between the excitation and response signals of the EIS data at 100 Hz after being processed with the IFFT.

Impedance tests were conducted under AC pulse signal excitation, with the frequency range of 0.1 to 1 kHz. As indicated in Figure 5E, the AC pulse signal exhibited multiple odd-order harmonic components after data processing, which decreased sequentially. To ensure the accuracy of subsequent EIS calculations, only the first three harmonics were selected for impedance data acquisition, implementing a one-to-three relationship. Impedance data testing was carried out using a fixed-frequency sweep measurement method, dividing the frequency range from 0.1 to 1 kHz into several segments with intervals in powers of 10. For example, within the range of 0.1 to 1 Hz, fixed frequency points of 0.1, 0.2, 0.4, 0.7, 0.8, and 0.9 were selected, with the next frequency segment being ten times the previous one, continuing up to the maximum frequency of 1 kHz. The AC pulse signal in the testing process effectively ensured that the SOC of LIBs remained unaltered, further guaranteeing the accuracy of the data.

When conducting EIS testing with AC pulse excitation signals, it is still necessary to adhere to the three conditions of EIS testing: causality, stability, and linearity [6]. Among these, the conditions of causality and stability are readily met. Causality refers to the requirement that the input perturbation signal and the output response signal are interrelated, meaning the perturbation signal's existence and the response signal's changes cannot be completely independent. Stability means that the system can return to its pre-disturbance state after the perturbation is applied [23]. The electrochemical impedance formula for the battery is:

$$Z = \Delta E / \Delta i \quad (8)$$

In the equation, the total current Δi is related to the concentration of species Δc_i and the potential ΔE as follows: i^n

$$\Delta i = \sum \left(\frac{\partial i}{\partial c_i} \right) \Delta c_i + \left(\frac{\partial i}{\partial E} \right) \Delta E + 0i^n \quad (9)$$

In the equation, $0i^n$ represents higher-order terms. By neglecting the higher-order terms, the transformed equation can be used to determine Z:

$$Z = 1 / \frac{\partial i}{\partial E} \left[1 - \sum \left(\frac{\partial i}{\partial c_i} \right) \frac{\Delta c_i}{\Delta i} \right] \quad (10)$$

Expanding Equation (10) at this point, the first term represents the charge transfer impedance ($R_{ct} = \partial E / \partial i$), while the second term involves the effects of both the electrolyte and electrode diffusion [40]. The total current of the charge transfer reaction occurring on

the electrode is related to the overpotential η_s , which can be derived from the Butler–Volmer equation as follows:

$$i = i_0 \left(\exp\left(\frac{(1-\alpha)nF\eta_s}{RT}\right) - \exp\left(-\frac{\alpha nF\eta_s}{RT}\right) \right) \quad (11)$$

In the equation, i_0 is the exchange current density, α is the charge transfer coefficient, F is the Faraday constant, R is the gas constant, and T is the absolute temperature. The overpotential η_s represents the degree of deviation from the equilibrium potential [41]. To make the chemical kinetics expressed by this equation more reasonable, Equation (11) can be represented in terms of the transfer coefficients for the anodic and cathodic reactions:

$$i = i_0 \left(\exp\left(\frac{\alpha_a F \eta_s}{RT}\right) - \exp\left(-\frac{\alpha_c F \eta_s}{RT}\right) \right) \quad (12)$$

Here, α_a and α_c are the anodic and cathodic transfer coefficients, respectively. The exchange current i_0 depends on the concentrations of the oxidized state c_O and the reduced state c_R in the charge transfer reaction. The expression is as follows:

$$i_0 = nFk_0(c_O - c_R) \quad (13)$$

The current density i can be expanded using a Taylor series as follows:

$$\left\{ (\alpha_a + \alpha_c) \frac{F \eta_s}{RT} + \frac{(\alpha_a^2 - \alpha_c^2)}{2} \left(\frac{F \eta_s}{RT} \right)^2 + \frac{(\alpha_a^3 - \alpha_c^3)}{6} \left(\frac{F \eta_s}{RT} \right)^3 + 0\eta_s^4 \dots + \frac{(\alpha_a^n - \alpha_c^n)}{n!} \left(\frac{F \eta_s}{RT} \right)^n \dots \right\} \quad (14)$$

In the above equation, with reference values $\alpha_a = \alpha_c = 0.5$ and $T = 298$ K, higher-order terms are considered infinitesimal. To ensure the equation is suitable for linear analysis, the current must be direct current, or its variation must be less than 1% [42]. Based on Ohm's law, it can be intuitively derived that the most commonly used response range at the steady-state operating point is around 5~40 mV [43]. Therefore, to meet the linearity condition mentioned above, and based on experimental comparisons, an AC pulse signal of approximately ± 1 A is found to be optimal for testing excitation signals, with the response voltage at the steady-state operating point controlled to around 40 mV.

To enhance the comparability of the experiments, EIS tests were conducted under different cycling conditions and various SOC in addition to the aforementioned aging experiments on LIBs. The results were also used to verify the accuracy of the designed EIS test apparatus and compared with tests conducted using traditional electrochemical workstations. These tests involved sinusoidal excitation signals with an amplitude of ± 1 A and a frequency range from 0.1 Hz to 1 kHz. The graphical representation of these experiments is presented in Figure 6.

In Figure 6A,B, the electrochemical workstation presents the data as smooth curves, whereas the EIS testing system displays them as discrete data points. Both in terms of the trend of changes and the magnitude of the data, there is little difference between the measurement results of the two systems. This confirms the accuracy of the EIS testing system in battery measurements. Regarding measurement time, the electrochemical workstation employs single-frequency sweep measurements, acquiring only one impedance data point at a time. When the frequency range is set from 0.1 Hz to 1 kHz, the measurement takes approximately 5 min. In contrast, when using the EIS testing system with AC pulse signals, it can simultaneously obtain one-to-three impedance data, thereby increasing the testing speed by nearly threefold. Furthermore, as observed in Figure 6C,D, the impedance data under different SOC conditions primarily differ in the magnitude of the arc portion. In

Figure 6E,F, impedance data under various cycle counts exhibit an overall rightward shift, with the degree of shift being associated with the number of cycles.

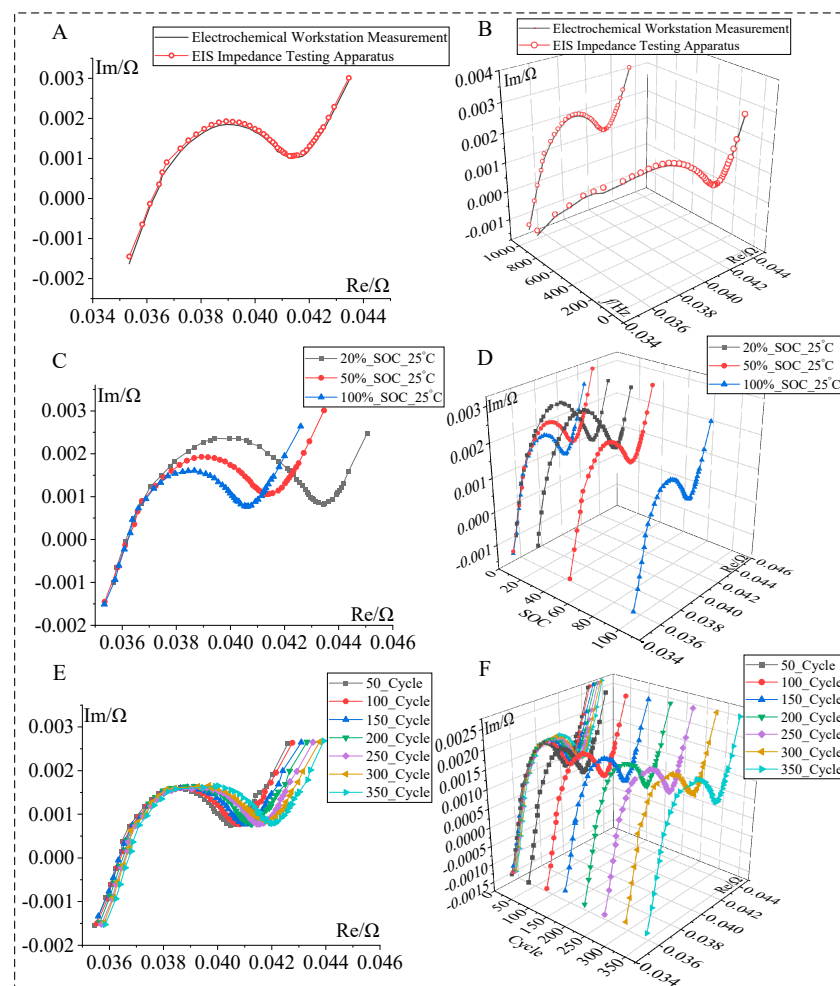


Figure 6. Impedance spectra at different SOC levels and under various cycle numbers. (A,B) Comparison between the EIS testing apparatus and the electrochemical workstation; (C,D) Impedance plots of different cycling numbers; (E,F) Impedance plots of different cycling numbers.

5. RDRT Impedance Data Processing and SOH Estimation

5.1. RDRT Impedance Data Processing

The conventional approach to EIS data processing involves fitting the data to a model. This method, however, cannot guarantee the quality of the assumed model and necessitates comparisons with different model assumptions or prior research. Additionally, this method fails to address fitting issues resulting from impedance data overlap [43]. In response to these limitations, this paper employs the RDRT method for impedance data processing. This method employs different time constants to represent various electrochemical reaction processes and manifests itself in peak form on the DRT impedance spectrum. This approach effectively compensates for the shortcomings of traditional EIS data fitting methods, enabling impedance data analysis without reliance on a specific model.

The comparative graphs of impedance data processed through RDRT under different SOC and different cycling numbers are presented in Figure 7, as illustrated. The horizontal axis in the graph represents the time constant τ/s , while the vertical axis represents the impedance magnitude $\gamma(\tau)/\Omega$. During the RDRT processing, the option to include inductance data in the DRT processing can be chosen, and the discretization method utilizes a Gaussian function with a regularization parameter λ set at 0.001. Therefore, Figure 7A,B

depicts DRT impedance graphs without inductance for different cycling numbers, while Figure 7C,D shows impedance without inductance. These correspond to six polarization processes associated with different electrochemical reactions. For LIBs at varying cycling numbers, these six electrochemical reactions remain consistent, but the impedance values vary under different electrochemical reactions. Similarly, Figure 7E,F represents DRT impedance graphs without inductance at different SOC levels, while Figure 7G,H shows impedance without inductance. It is worth noting that S_3 is present only at low SOC levels and not S_7 . In summary, the impedance values corresponding to S_2 , S_5 , S_6 , and S_7 are significantly affected by SOC, whereas the impedance values for S_1 , S_3 , and S_4 are less influenced by SOC.

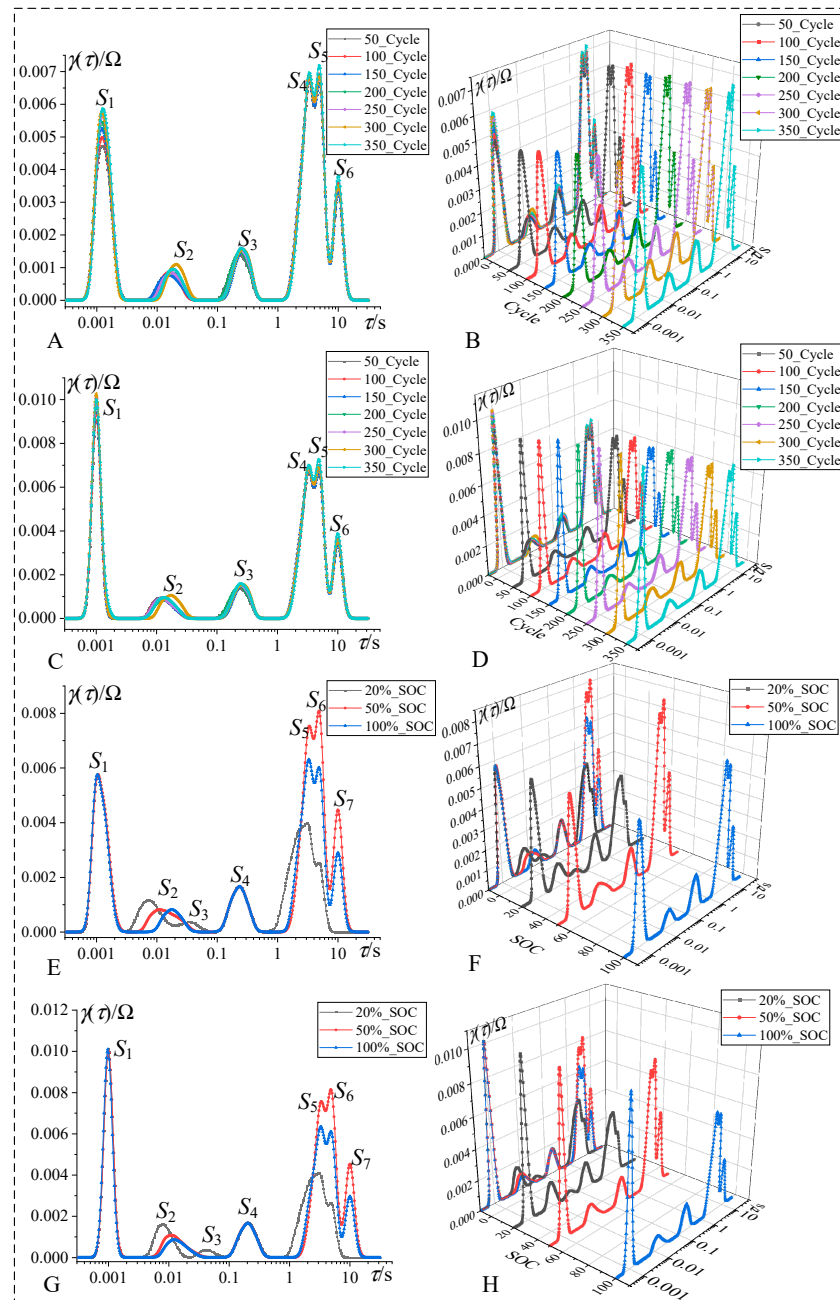


Figure 7. Comparison plots of impedance data processed with RDRT for different SOC and cycle numbers. (A,B) DRT impedance plots without inductance at different cycling numbers; (C,D) DRT impedance plots with inductance at different cycling numbers. (E,F) DRT impedance plots without inductance at various SOC levels. (G,H) DRT impedance plots with inductance at various SOC levels.

In summary, the inclusion of inductance data does not affect the polarization processes in the impedance data processed by the RDRT method. The changes are primarily reflected in the magnitude of the impedance values. Furthermore, the time constants τ corresponding to the polarization processes S_1 and S_3 in Figure 7A–D are the same as those for the polarization processes S_1 and S_4 in Figure 7E–H, indicating that they correspond to the same electrochemical reactions. These two polarization processes are less influenced by SOC changes, and their DRT impedance values exhibit consistent patterns across different cycling numbers. Additionally, the impedance values for S_1 and S_3 show significant differences under varying cycling numbers and SOC levels. Therefore, it is initially possible to estimate the state of health (SOH) of lithium-ion batteries based on the impedance characteristics at the time constants associated with S_1 and S_3 .

5.2. Estimation of SOH for LIBs

By employing the aforementioned RDRT method to process EIS data obtained under different SOC and cycling numbers, we can deduce the impedance characteristics associated with S_1 and S_3 for estimating the SOH of LIBs at various cycling stages. The impedance values corresponding to S_1 and S_3 are provided in Table 1, where $S_1/\gamma(\tau)$ and $L_S_1/\gamma(\tau)$ represent the impedance values associated with time constants in the presence or absence of inductance data. Furthermore, the calculation of LIBs SOH is based on the ratio of the current maximum discharge capacity (C_{now}) to the rated capacity (C_{max}):

$$SOH = \frac{C_{now}}{C_{max}} \cdot 100\% \quad (15)$$

Table 1. DRT impedance data at various cycle numbers.

| Actual SOH Value | Cycle | $S_1/\gamma(\tau) \Omega$ | $S_3/\gamma(\tau) \Omega$ | $L_S_1/\gamma(\tau) \Omega$ | $L_S_3/\gamma(\tau) \Omega$ |
|------------------|-------|---------------------------|---------------------------|------------------------------|------------------------------|
| 98.86% | 50 | 0.00475 | 0.00137 | 0.00908 | 0.00137 |
| 96.95% | 100 | 0.00499 | 0.00145 | 0.0094 | 0.00144 |
| 95.89% | 150 | 0.00532 | 0.00148 | 0.00982 | 0.00148 |
| 94.59% | 200 | 0.00546 | 0.00149 | 0.00997 | 0.00151 |
| 93.34% | 250 | 0.00566 | 0.00153 | 0.01016 | 0.00153 |
| 92.45% | 300 | 0.00573 | 0.00155 | 0.01027 | 0.00155 |
| 91.23% | 350 | 0.00585 | 0.0016 | 0.00999 | 0.00159 |

From the obtained data, we can observe that as the cycle number increases or SOH decreases, the impedance values corresponding to S_1 and S_3 show an increasing trend. Therefore, these two parameters to some extent reflect the relationship between impedance and SOH, making them suitable as state characterization parameters for assessing the aging condition of LIBs.

To enhance the visibility of the changes in impedance data corresponding to S_1 and S_3 with respect to SOH and cycle number variations, their trending plots are shown in Figure 8.

According to the impedance data trends corresponding to S_1 and S_3 under different cycling numbers as mentioned above, we have established an empirical model for the lifetime degradation in the form of a polynomial, with its basic formula as follows: $y = b + ax + cx^2 + \dots$, where y represents the aging characterization parameter, and x corresponds to the aging cycle number in the experiment. By utilizing the data above, we determine the unknown variables in the aging model formula and then reverse-map to obtain the estimated SOH for the corresponding cycle numbers. To assess the goodness of fit of the empirical model for lifetime degradation with the characterization parameter, we introduce the R^2 . $R^2 \in (0 \sim 1)$, where a higher R^2 value indicates a better fit for the

model and a more accurate prediction of future data trends [41,44]. The formula for R^2 is as follows:

$$\left\{ \begin{array}{l} R^2 = 1 - RSS/TSS \\ RSS = \sum_{i=1}^n (y_i - y'_i)^2 \\ TSS = \sum_{i=1}^n (y_i - \bar{y})^2 \end{array} \right. \quad (16)$$

In the above equation, y_i represents the i th raw data, y'_i is the calculated value from the aging model, \bar{y} represents the mean of the raw data, and n is the number of fitted data points. The R^2 values under different lifetime degradation empirical models are shown in Table 2.

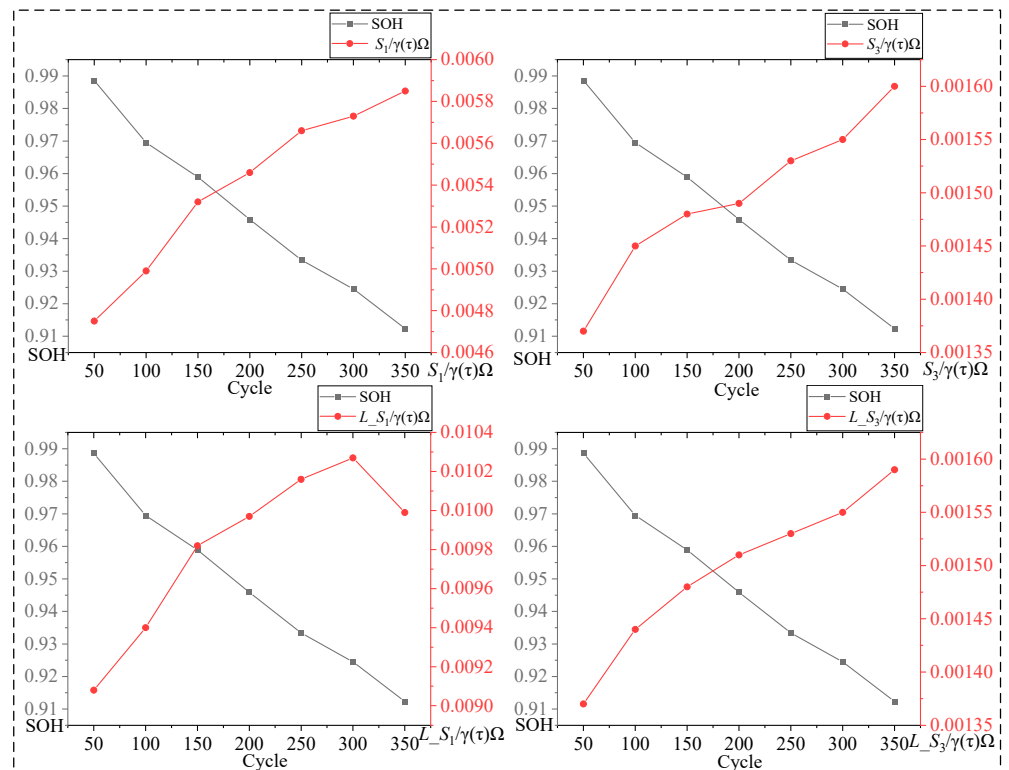


Figure 8. Investigation of the impedance data trends corresponding to S_1 and S_3 at different cycle numbers.

Table 2. The R^2 for different empirical models of aging degradation.

| SOC | The Parameters | First-Order Model of R^2 | Second-Order Model of R^2 | Third-Order Model of R^2 |
|------|----------------------------|----------------------------|-----------------------------|----------------------------|
| 100% | $S_1/\gamma(\tau) \Omega$ | 0.976 | 0.992 | 0.996 |
| | $S_3/\gamma(\tau) \Omega$ | 0.921 | 0.950 | 0.987 |
| | $L_S1/\gamma(\tau) \Omega$ | 0.903 | 0.979 | 0.986 |
| | $L_S3/\gamma(\tau) \Omega$ | 0.918 | 0.986 | 0.995 |

In the above table, R^2 represents the average goodness of fit for each group under 350 cycles and is considered the optimal combination. It can be inferred that as the order of the life degradation empirical model increases, the goodness of fit improves; however, the computational workload also increases exponentially. Furthermore, in the second-order life degradation empirical model, the impedance data corresponding to S_1 provides the best goodness of fit. In summary, using S_1 impedance data as a characterization parameter, combined with the second-order life degradation empirical model, represents the optimal

approach for estimating the state of health (SOH) of lithium-ion batteries (LIBs). This method offers an effective balance between computational efficiency and accuracy. The SOH estimation process involves utilizing the data from Table 1 to determine the function that relates the S_1 impedance data to the actual SOH as a function of the number of cycles. Subsequently, this function is used to estimate the number of cycles based on the S_1 impedance data. Finally, the estimated SOH values for different cycle counts are obtained. The results of SOH estimation for S_1 impedance data under the second-order life degradation empirical model are presented in Table 3.

Table 3. SOH estimation results of S_1 impedance data under the second-order aging degradation empirical model.

| SOC | Cycle | Actual SOH Value | Estimated SOH Value | Absolute Error |
|------|-------|------------------|---------------------|----------------|
| 100% | 50 | 98.86% | 97.284% | 1.576% |
| | 100 | 96.95% | 96.062% | 0.889% |
| | 150 | 95.89% | 93.988% | 1.902% |
| | 200 | 94.59% | 93.363% | 1.227% |
| | 250 | 93.34% | 91.949% | 1.391% |
| | 300 | 92.45% | 91.322% | 1.128% |
| | 350 | 91.23% | 89.902% | 1.328% |

From the final state of health (SOH) estimation results presented in Table 3, it is evident that the absolute error remains within 2%, and the overall SOH estimation process is user-friendly, with no need to be concerned about the quality of the fitting model. In terms of computational load, it is significantly lower compared to data-driven approaches, as noted in reference [45], while maintaining higher accuracy when compared to SOH estimation errors based on equivalent circuit models of electrochemical impedance spectroscopy (EIS), which exhibit an error rate of 4% [46].

6. Conclusions

This study addresses the safety hazards and performance degradation issues that lithium-ion batteries may encounter in practical applications. In response to the limitations of conventional EIS testing methods, such as slow speed, insufficient flexibility, and practical implementation challenges, an innovative design for a fast EIS testing system is proposed. The proposed system integrates alternating current pulse excitation signals with an “FFT intelligent optimization algorithm”, enabling a “one-to-many” acquisition of impedance data. This significantly improves testing efficiency while ensuring measurement accuracy. Furthermore, to address the ambiguity caused by overlapping impedance spectra, this study introduces and validates a novel RDRT method for data processing, effectively avoiding analysis uncertainty associated with assumptions about equivalent circuit models. This technological improvement not only enhances the system’s operational efficiency but also provides new insights into lithium-ion battery testing, with promising applications in energy storage, smart grids, and new energy vehicles.

In experimental validation, the study successfully extracted effective parameters and reliably estimated the state of health (SOH) by comparing the DRT impedance spectra under different states of charge (SOC) and cycle numbers, with an absolute error controlled within 2%, demonstrating the system’s technical feasibility and application value. These results not only verify the innovative potential of the proposed fast EIS testing system but also provide theoretical support and practical guidance for the safe operation, state monitoring, and reuse of lithium-ion batteries.

The research concludes that the EIS fast testing system based on the variable excitation balancing board demonstrates significant application potential in the field of lithium-ion battery energy storage. This system provides efficient data acquisition and analysis support for the state estimation and second-life utilization of lithium-ion batteries while playing a key role in ensuring safety in practical applications. Given the widespread use of lithium-ion batteries in energy storage, smart grids, and new energy vehicles, this research will inject new momentum into the technological development of related fields, while advancing lithium-ion battery technology toward higher-level applications.

Author Contributions: Conceptualization, L.W. and H.C.; methodology, H.C.; software, J.B.; validation, H.C., Z.W. and J.B.; formal analysis, B.Z.; investigation, C.F.; data curation, Z.W.; writing—original draft preparation, H.C.; writing—review and editing, L.W.; visualization, Z.S.; supervision, Y.Z.; project administration, L.W.; funding acquisition, L.W. All authors have read and agreed to the published version of the manuscript.

Funding: This research was funded by the National Key Research and Development Program of China, grant number 2023YFB2406000, Scientific and Technological Research Project of the Hubei Provincial Department of Education, grant number D20231405 and Knowledge Innovation Program of Wuhan-Shuguang Project, grant number 2023010201020372.

Data Availability Statement: The original contributions presented in the study are included in the article, further inquiries can be directed to the corresponding author.

Acknowledgments: The author is grateful for the review and guidance of the reviewing experts. At the same time, the author would also like to thank the Hubei Key Laboratory for High-efficiency Utilization of Solar Energy and Operation Control of Energy Storage System for its support.

Conflicts of Interest: Authors Chunxia Fu and Lujun Wang were employed by the Powerchina Equipment Research Institute Co., Ltd. Author Yunbin Zhang was employed by the company Hubei New Energy Co., Ltd. The remaining authors declare that the research was conducted in the absence of any commercial or financial relationships that could be construed as a potential conflict of interest.

References

1. Shen, J.; Ma, W.; Shu, X.; Shen, S.; Chen, Z.; Liu, Y. Accurate state of health estimation for lithium-ion batteries under random charging scenarios. *Energy* **2023**, *279*, 128092. [[CrossRef](#)]
2. Bian, X.; Liu, L.; Yan, J. A model for state-of-health estimation of lithium-ion batteries based on charging profiles. *Energy* **2019**, *177*, 57–65. [[CrossRef](#)]
3. Yu, Q.; Nie, Y.; Liu, S.; Li, J.; Tang, A. State of health estimation method for lithium-ion batteries based on multiple dynamic operating conditions. *J. Power Sources* **2023**, *582*, 233541. [[CrossRef](#)]
4. Chao, L.; Zhang, T.; Luo, W.; Wei, G. SOH estimation of lithium-ion batteries based on fast time domain impedance spectroscopy. In Proceedings of the 2019 14th IEEE Conference on Industrial Electronics and Applications (ICIEA), Xi'an, China, 19–21 June 2019; IEEE: New York, NY, USA, 2019.
5. Wei, G. Design of Rapid State Evaluation System for Lithium-Ion Battery Based on Impedance Spectroscopy. Master's Thesis, Harbin Institute of Technology, Harbin, China, 2020.
6. Cao, C.; Zhang, J. *An Introduction to Electrochemical Impedance Spectroscopy*; Science Press: Beijing, China, 2016; pp. 20–36. (In Chinese)
7. Wen, J.; Chen, X.; Li, X.; Li, Y. SOH prediction of lithium battery based on IC curve feature and BP neural network. *Energy* **2022**, *261*, 125234. [[CrossRef](#)]
8. Ren, Z.; Du, C. A review of machine learning state-of-charge and state-of-health estimation algorithms for lithium-ion batteries. *Energy Rep.* **2023**, *9*, 2993–3021. [[CrossRef](#)]
9. Luo, F.; Huang, H.; Wang, H. Rapid prediction of the state of charge and state of health of decommissioned power batteries based on electrochemical impedance spectroscopy. *Chin. J. Sci. Instrum.* **2021**, *42*, 172–180.
10. Angst, U.M.; Elsener, B. Measuring corrosion rates: A novel AC method based on processing and analysing signals recorded in the time domain. *Corros. Sci.* **2014**, *89*, 307–317. [[CrossRef](#)]
11. Hoshi, Y.; Yakabe, N.; Isobe, K.; Saito, T.; Shitanda, I.; Itagaki, M. Wavelet transformation to determine impedance spectra of lithium-ion rechargeable battery. *J. Power Sources* **2016**, *315*, 351–358. [[CrossRef](#)]

12. Arora, S.; Shen, W.; Kapoor, A. Review of mechanical design and strategic placement technique of a robust battery pack for electric vehicles. *Renew. Sustain. Energy Rev.* **2016**, *60*, 1319–1331. [[CrossRef](#)]
13. Lindahl, P.A.; Cornachione, M.A.; Shaw, S.R. A time-domain least squares approach to electrochemical impedance spectroscopy. *IEEE Trans. Instrum. Meas.* **2012**, *61*, 3303–3311. [[CrossRef](#)]
14. Kallel, A.Y.; Kanoun, O. On the design of multisine signals for maintaining stability condition in impedance spectroscopy measurements of batteries. *J. Energy Storage* **2023**, *58*, 106267. [[CrossRef](#)]
15. Bullecks, B.; Suresh, R.; Rengaswamy, R. Rapid impedance measurement using chirp signals for electrochemical system analysis. *Comput. Chem. Eng.* **2017**, *106*, 421–436. [[CrossRef](#)]
16. Du, X.; Meng, J.; Peng, J.; Liu, Y. A novel lithium-ion battery impedance fast measurement method with enhanced excitation signal. *IEEE Trans. Ind. Electron.* **2023**, *70*, 12322–12330. [[CrossRef](#)]
17. Xiong, R.; Tian, J.; Mu, H.; Wang, C. A systematic model-based degradation behavior recognition and health monitoring method for lithium-ion batteries. *Appl. Energy* **2017**, *207*, 372–383. [[CrossRef](#)]
18. Wang, J.; Huang, Q.; Li, W.; Wang, J.; Zhuang, Q.; Zhang, J. Basis of relaxation time distribution by electrochemical impedance spectroscopy. *J. Electrochem.* **2020**, *26*, 607–627.
19. Chang, C.; Wang, S.; Tao, C.; Jiang, J.; Jiang, Y.; Wang, L. An improvement of equivalent circuit model for state of health estimation of lithium-ion batteries based on mid-frequency and low-frequency electrochemical impedance spectroscopy. *Measurement* **2022**, *202*, 111795. [[CrossRef](#)]
20. Huang, J.; Li, Z.; Zhang, J.; Song, S.; Lou, Z.; Wu, N. An analytical three-scale impedance model for porous electrode with agglomerates in lithium-ion batteries. *J. Electrochem. Soc.* **2015**, *162*, A585. [[CrossRef](#)]
21. Jiang, B.; Zhu, J.; Wang, X.; Wei, X.; Shang, W.; Dai, H. A comparative study of different features extracted from electrochemical impedance spectroscopy in state of health estimation for lithium-ion batteries. *Appl. Energy* **2022**, *322*, 119502. [[CrossRef](#)]
22. Li, D.; Yang, D.; Li, L.; Wang, L.; Wang, K. Electrochemical impedance spectroscopy based on the state of health estimation for lithium-ion batteries. *Energies* **2022**, *15*, 6665. [[CrossRef](#)]
23. Timothy, L.S. *The Power Electronics Handbook*, 1st ed.; CRC Press: Boca Raton, FL, USA, 2018.
24. Wang, C.; Ye, S.; Pei, C.; Dai, C. Review on battery state-of-health experiment and estimation methods. *Battery Bimon.* **2021**, *51*, 197–200.
25. Popkirov, G.S.; Schindler, R.N. A new impedance spectrometer for the investigation of electrochemical systems. *Rev. Sci. Instrum.* **1992**, *63*, 5366–5372. [[CrossRef](#)]
26. Orazem, M.E.; Tribollet, B. *Electrochemical Impedance Spectroscopy*, 1st ed.; John Wiley & Sons, Inc.: Hoboken, NJ, USA, 2008.
27. Shi, W.; Jia, C.; Zhang, Y.; Lü, Z.; Han, M. Differentiation and decomposition of solid oxide fuel cell electrochemical impedance spectra. *Acta Phys. Chim. Sin.* **2019**, *35*, 509–516. [[CrossRef](#)]
28. Fuoss, R.M.; Kirkwood, J.G. Electrical properties of solids. VIII. Dipole moments in polyvinyl chloride-diphenyl systems. *J. Am. Chem. Soc.* **1941**, *63*, 385–394. [[CrossRef](#)]
29. Wang, S.; Yan, S.; Li, H.; Wang, K.; Jiang, K. Distribution of relaxation times analysis from battery impedance spectroscopy using regularization method. *Proc. CSEE* **2022**, *42*, 3177–3188.
30. Schiclein, H.; Müller, A.C.; Voigts, M.; Krügel, A.; Ivers-Tiffée, E. Deconvolution of electrochemical impedance spectra for the identification of electrode reaction mechanisms in solid oxide fuel cells. *J. Appl. Electrochem.* **2002**, *32*, 875–882. [[CrossRef](#)]
31. Saccoccio, M.; Wan, T.H.; Chen, C.; Ciucci, F. Optimal regularization in distribution of relaxation times applied to electrochemical impedance spectroscopy: Ridge and lasso regression methods—A theoretical and experimental study. *Electrochim. Acta* **2014**, *147*, 470–482. [[CrossRef](#)]
32. Wan, T.H.; Saccoccio, M.; Chen, C.; Ciucci, F. Influence of the discretization methods on the distribution of relaxation times deconvolution: Implementing radial basis functions with DRTtools. *Electrochim. Acta* **2015**, *184*, 483–499. [[CrossRef](#)]
33. Boukamp, B.A. Fourier transform distribution function of relaxation times; application and limitations. *Electrochim. Acta* **2015**, *154*, 35–46. [[CrossRef](#)]
34. Tesler, A.B.; Lewin, D.R.; Baltianski, S.; Tsur, Y. Analyzing results of impedance spectroscopy using novel evolutionary programming techniques. *J. Electroceramics* **2010**, *24*, 245–260. [[CrossRef](#)]
35. Li, X.; Ahmadi, M.; Collins, L.; Kalinin, S.V. Deconvolving distribution of relaxation times, resistances, and inductance from electrochemical impedance spectroscopy via statistical model selection: Exploiting structural-sparsity regularization and data-driven parameter tuning. *Electrochim. Acta* **2019**, *313*, 570–583. [[CrossRef](#)]
36. Valiūnienė, A.; Sabirovas, T.; Petronienė, J.; Ramanavičius, A. Towards the application of fast Fourier transform-scanning electrochemical impedance microscopy (FFT-SEIM). *J. Electroanal. Chem.* **2020**, *864*, 114067. [[CrossRef](#)]
37. Kramers, H.A. La diffusion de la lumière par les atomes. In Proceedings of the Volta Centenary Congress, Como, Italy, 11 September 1927; Volume 2, pp. 545–557.
38. Kronig, R.L. On the theory of dispersion of X-rays. *J. Opt. Soc. Am.* **1926**, *12*, 547–557. [[CrossRef](#)]
39. GB/T 18287-2000; General Specification of Lithium-Ion Batteries for Cellular Phones. Standards Press of China: Beijing, China, 2000.

40. Brivio, C.; Musolino, V.; Merlo, M.; Ballif, C. A physically-based electrical model for lithium-ion cells. *IEEE Trans. Energy Convers.* **2019**, *34*, 594–603. [[CrossRef](#)]
41. Rahn, C.D.; Wang, C.Y. *Battery Systems Engineering*; John Wiley & Sons Ltd.: Oxford, UK, 2013.
42. Wojcik; Orazem, M.E. Variable-amplitude galvanostatically modulated impedance spectroscopy as a tool for assessing reactivity at the corrosion potential without distorting temporal evolution of the system. *Corros. J. Sci. Eng.* **1998**, *54*, 289–298. [[CrossRef](#)]
43. Zhou, X.; Huang, J.; Pan, Z.; Ouyang, M. Impedance characterization of lithium-ion batteries aging under high-temperature cycling: Importance of electrolyte-phase diffusion. *J. Power Sources* **2019**, *426*, 216–222. [[CrossRef](#)]
44. Wang, X.; Li, R.; Wei, X.; Dai, H.; Zheng, Y. Study on remaining useful life prediction of lithium-ion batteries based on charge transfer resistance. *J. Mech. Eng.* **2021**, *57*, 105–117.
45. Chen, X.; Hu, Y.; Li, S.; Wang, Y.; Li, D.; Luo, C.; Xue, X.; Xu, F.; Zhang, Z.; Gong, Z.; et al. State of health (SOH) estimation and degradation modes analysis of pouch NMC532/graphite Li-ion battery. *J. Power Sources* **2021**, *498*, 229884. [[CrossRef](#)]
46. Wang, S.; Wu, X.; Bai, Z. A method for estimating the state of health of retired lithium batteries. *Mech. Sci. Technol. Aerosp. Eng.* **2021**, *105*, 1–11.

Disclaimer/Publisher’s Note: The statements, opinions and data contained in all publications are solely those of the individual author(s) and contributor(s) and not of MDPI and/or the editor(s). MDPI and/or the editor(s) disclaim responsibility for any injury to people or property resulting from any ideas, methods, instructions or products referred to in the content.